Preparation of hierarchical porous carbon through one-step KOH activation of coconut shell biomass for high-performance supercapacitor

Yutong Zhao
Northeast Petroleum University
Yuanyuan Wang
Northeast Petroleum University
Yanxiu Liu
Northeast Petroleum University
Huan Wang
Northeast Petroleum University
Hua Song (songhua2004@sina.com)
Northeast Petroleum University

Research Article

Keywords: Biomass, Porous carbon, KOH activation, Coconut shell carbon, Supercapacitor

Posted Date: August 2nd, 2022

DOI: https://doi.org/10.21203/rs.3.rs-1895857/v1

Abstract

Here we report an effective and facile method for preparing porous carbons (CSCK-T-*x*) with highly developed hierarchical porosity for high-performance supercapacitor by one-step KOH activation of coconut shell carbon. The effects of carbonization temperature (T, ^{o}C) and KOH/C ratio (*x*) on the structure and electrochemical properties were studied systematically. The as-prepared CSCK-800-2 displayed two concentrated mesopores at 4 nm and 14 nm. The unique hierarchical structure of CSCK-800-2 enables it to have low ion transport resistance and high ion-accessible surface area, which contributes to outstanding electrochemical performance. Furthermore, it possessed the highest BET specific surface area of 2143.6 $m^2 \cdot g^{-1}$ with a pore volume of 1.34 $cm^3 \cdot g^{-1}$ among the CSCK-T-*x*. In a three-electrode test system, CSCK-800-2 exhibits a high specific capacitance of 317 $F \cdot g^{-1}$ at a current density of 0.5 $A \cdot g^{-1}$ and considerable rate retention of 68% at 20 $A \cdot g^{-1}$. The symmetrical supercapacitor that was based on CSCK-800-2 showed a maximum energy density of 13.5 $Wh \cdot kg^{-1}$ at 0.5 $A \cdot g^{-1}$ in 6M KOH electrolyte. Besides, it also exhibited a superior cycling stability with 99.7% of the capacitance retention after 10000 cycles at 5 $A \cdot g^{-1}$.

1. Introduction

With the increasing demand for energy from transportation electrification and smart grids, as well as the gradual depletion of fossil fuels, it is significant to develop efficient, low cost, eco-friendly and high-performance energy storage equipments [1]. Supercapacitors (SCs) have received extensive attention for their excellent cycling stability and high power density. [2]. However, its low energy density has become a key factor restricting its wider development. Therefore, it is necessary to improve the energy density of SCs to satisfy urgent demand for uninterruptible power supplies. The charge storage mechanisms of SCs can be divided into the electric double-layer capacitors (EDLC) which rely on electrostatic attractions between ions and charged electrode surface, such as carbon materials [3]; and pseudo capacitance based on the highly reversible redox reactions on the surface or in the bulk phase of the electrode materials, such as transition metal oxides [4], transition metal hydroxides [5] and conductive polymers [6].

Many factors contribute to the performance of SCs, such as the electrochemical performance of electrode materials, electrolyte selection and potential window of the electrode, etc. Among these factors, the performance of electrode material is the most important factors affecting its electrochemical performance. In EDLC phenomenon, ion interaction between electrode/electrolyte interfaces is essential for efficient charge-discharge process. The electrode material needs to have large specific surface area and reasonable pore structure to maximize the charge storage density of SCs Some advanced materials including metal oxides [6], conductive polymers [4, 5], and carbon-based materials are reported [7–10]. Among these materials, carbon-based materials have attracted widespread attention for their large specific surface area, low cost, wide sources, non-toxic and high electrical conductivity [11, 12]. However, their theoretical capacity and energy density have not reached a satisfactory level. An effective way to solve the above problem is to construct hierarchical porous structure which is beneficial to high-density

charge storage. [13–15]. Micropores (< 2 nm) can enhance surface area to ensure high energy storage capacity, small mesopores (between 4 and 6 nm) increase ion-accessible surface area with a lower ion-transport resistance, large mesopores (between 10 and 50 nm) and macropores (> 50 nm) act as ion buffering reservoir to shorten ion-transport pathway and reduce the resistance of electron transport [16–18]. In conclusion, those carbon-based electrode materials with suitable hierarchical porous structure and high surface areas are ideal for EDLCs. However, some micropores whose sizes do not match the size of electrolyte ion or too much large mesopores, which usually lead to poor capacity and relatively low specific surface area [19, 20].

A variety of methods, including physical and chemical activation, have been tried to obtain the ideal porous structure. Chemical activation creates pores by etching or reacting with carbon and is more efficiently than physical activation [21]. In general, chemicals such as KOH, K_2CO_3, KCl, and $ZnCl_2$, etc. are mixed with biochar or carbon materials for high-temperatures pyrolysis under inert atmosphere [22–24]. At high temperatures, a varity of chemical and physical reactions take place to produce porous structures through etching and gasification effect [25]. KOH activation is considered to be the most effective chemical activation method. In addition, carbon source is also a critical factor restricting industrial application. Recently, the carbon nanotubes, graphene, carbon aerogels and porous carbons are widely used as high-performance supercapacitor electrodes [14, 26, 27]. Among these materials, the nanoporous carbon electrodes obtained from natural biomass are more eco-friendly, cost-effective and renewable. For example, Yin et al. [28] synthesized porous carbon electrode from coconut shell by using carbon dioxide and potassium hydroxide as physical activator and chemical activator. The materials exhibited a high specific capacitance of 266 $F \cdot g^{-1}$ at 0.1 $A \cdot g^{-1}$ with a specific surface area of 2898 $m^2 \cdot g^{-1}$. Bai et al. [29] fabricated N/O co-doped activated carbon from glucose as raw materials without using any toxic reagents. Its energy density was 17.1 $Wh \cdot kg^{-1}$, and the cyclic stability reached 88.1% after 10000 cycles. Wang et al. [30] prepared rod-like activated carbon by KOH activation using aniline-modified lignin. The materials showed high specific surface area with connected cavities, which lead to the specific capacitance of 336 $F \cdot g^{-1}$ and good electrochemical performance.

Coconut shell is mainly consists of cellulose, lignin and pentosan. It is a low-cost and renewable agricultural waste, which is widely distributed on the earth. For these reasons, coconut shell is a promising candidate for preparing porous carbon precursors [31]. The coconut shell-based activated carbons have been widely used as adsorbents for water and air treatments [32, 33], reduced graphenes [34], and electrodes [35]. Compared to other agricultural waste materials used as electrodes for supercapacitors, this activated carbon has large surface area, hierarchical porosity, as well as high conductivity [36–39]. Herein, a simple and effective method for preparing porous carbon with high hierarchical porosity by one-step activation of coconut shell carbon with KOH is proposed. The activated carbon exhibits a high specific surface area up to 2143.6 $m^2 \cdot g^{-1}$ with a unique hierarchical porous structure, a remarkable electrochemical performance with extraordinary cycling stability, showing that our work provides a sustainable and facile strategy for preparing porous carbon materials with promising applications in SCs.

2. Experiment

2.1 Materials

Coconut shell carbon was purchased from Wenxian Boyuan activated carbon factory. Potassium hydroxide (KOH), muriatic acid (HCl) and N-Methyl-2-pyrrolidinone (NMP) were purchased from Tianjin Damao Chemical Reagent Factory. Poly (vinylidene fluoride) (PVDF) was purchased from Aladdin Reagent Co., Ltd. Carbon black were acquired by Cabot Investment Co., Ltd. The carbon cloth (WOS 1009, CC) was purchased from the Taiwan carbon energy corporation.

2.2 Material Synthesis

The coconut shell carbon was ultrasonically cleaned with distilled water for 10 min, filtered and dried at 80 ^{o}C for 24h to obtain the pre-treated coconut shell carbon (CSC). Afterwards, the obtained black powder was added into KOH solution at a KOH/C ratio of x (x = 0.5, 1, 2, or 3; w/w). Then, the black paste was dried at 80 ^{o}C for 12h to remove redundant water and further grounded to ensure KOH was mixed evenly. Subsequently, the resultant mixture was placed in a nickel crucible and carbonized at different temperature (700, 800 and 900°C) for 2 h under N_2 atmosphere and cooled down to room temperature. After that, the samples were cleaned by 1M HCl and deionized water several times until the filtrate was neutral. Lastly, the synthesized coconut shell carbon was dried at 80 ℃ for over 12 h. The dried materials were labeled as CSCK-T-x (T = final activation temperature, x = weight ratio of KOH and C).

2.3 Characterization

A scanning electron microscope (SEM) with energy disperse spectroscopy (EDS) mapping was performed by SIGMA scanning electron microscope from Carl Zeiss AG, Germany, and the sample was magnified to 2000-10,000 times. The X-ray diffraction (XRD) analysis was recorded on a D/max2200PC-X-ray diffractomerter using Cu kα radiation. The specific surface area was measured by Brunauer-Emmett-Teller (BET) method, and the pore size distribution was calculated by classic Barrett-Joyner-Halenda (BJH) model. The characteristic peaks of carbon samples were identified by XploRA Plus (Jobionyvon Technology) for Raman spectra. X-ray photoelectron spectroscopy (XPS) was used for chemical element analysis and obtained by ESCALAB MKII spectrometer equipped with a hemispherical analyzer under vacuum conditions using the Mg radiation (E = 1253.6 eV).

2.4 Electrochemical measurements

The electrochemical test was carried out at the electrochemical workstation (Chenhua CHI660E, Shanghai) with 6M KOH as electrolyte. In the three electrode system, Pt sheet were used as the counter electrode and Hg/Hg_2Cl_2 as the reference electrode. The working electrode was fabricated as follows. Mix the active materials, polyvinylidene fluoride (PVDF), and carbon black in the mass ratio of 8: 1: 1, and added an appropriate amount of N-methylpyrrolidone (NMP) to form a uniform slurry. Then the sticky slurry was coated onto 1 cm^2 carbon cloth and dried at 80 ℃ in oven for 12h. Cyclic voltammetry (CV)

test was carried out in the potential range of -1-0 V at a series of scan rates from 5 to 200 mV s^{-1}. The galvanostatic charge–discharge (GCD) measurement was operated at different current density from 0.5 to 20 A g^{-1} with a potential window of -1-0 V. Electrochemical impedance spectroscopy (EIS) was conducted in a frequency range from 10^{-1} to 10^{5} Hz with an amplitude of 5 mV. In addition, the electrochemical measurement of symmetrical SCs was carried out by using a two-electrode system. The gravimetric specific capacitance (C, F·g^{-1}) of the electrode composites based on the three-electrode system and symmetric supercapacitors were calculated from galvanostatic charge-discharge (GCD) curve profiles according to the following eqation:

$$\mathrm{C} = \frac{I\Delta t}{m\Delta V}$$

1

Where I (A), Δt (s), ΔV (V) and m (g) refers to the discharge current, discharge time, potential change within Δt, and mass of the active material loaded in the working electrode, respectively.

Gravimetric energy density (E) in two-electrode system was evaluated through the equation below.

$$\mathrm{E}=\frac{\mathrm{C}\times\Delta\mathrm{V}^{2}}{2\times3.6}$$

2

Gravimetric power density (P) in two-electrode system was evaluated through the equation below:

$$\mathrm{P}=\frac{3600\mathrm{E}}{\Delta\mathrm{t}}$$

3

Where C represents the specific capacitance, ΔV refers to working potential, and t is the discharge time of symmetric supercapacitors.

3. Results And Discussion

3.1 Materials characterization

3.1.1 SEM analysis

Figure 1 shows the microstructural properties of the carbon samples. It can be observed from Fig. 1(a) and 1(b) that CSC is composed of numerous irregularly shaped objects with rough surface and no obvious pores. However, the obtained CSCK-800-2 presents a 3D structure with rich connected holes and thin hole walls (Fig. 1(c) and 1(d)). The differences in the micromorphology and microstructure of CSC

and CSCK-2-800 materials possibly because KOH can better enter the inner part of activated carbon to expand the pores and etch the material through oxidizing part of carbon into carbonate and oxycarbide at high temperature. It is beneficial to obtain better pore size distribution and more reasonable rational pore structure, which is conducive to providing more ion adsorption sites and reducing diffusion resistance [40]. In addition, the EDS spectrum (Fig. 1(e)) and element mapping showed that the C (Fig. 1(f)) and O (Fig. 1(g)) atoms are uniformly distributed.

3.1.2 XRD analysis

Figure 2 shows the XRD patterns of all samples. Two evident diffraction peaks at around 21° and 43° belong to the (002) and (100) planes of the graphitic structure, respectively. [41]. The broader peak around 21° indicates a certain degree of graphitization structure [42, 43]. At the activation temperature of 800 ℃, the peak of the samples becomes mild with the increase of KOH/C ratio. This shows that during the treatment of KOH activation, the activated carbon is continuously etched and the amorphous degree of CSCK-800-*x* continuously increased. This induces a better electrostatic adsorption and desorption of electrolyte ions in materials, and their electrochemical performance becomes more excellent. The weak peak at 2θ = 43° suggests that the existence of graphitic-type carbon frameworks in as-prepared CSCK-T-*x*. The peak intensity at 43° is gradually increased with the increase of activation temperature from 700 ^{o}C to 900 ^{o}C, demonstrating that the graphitization of CSCK-T-2 can be effectively improved by high activation temperature [44, 45].

3.1.3 Raman analysis

Figure 3 displays the Raman spectra of all samples. Two obvious peaks in the spectra were found at 1360 cm^{-1} and 1610 cm^{-1}, respectively, corresponding to the D band and G band [46]. The D band reflected the degree of disorder with substantial defects, and the G band revealed the E_2g vibration mode of graphitizaion carbon [47, 48]. The intensity ratio of D and G bands (I_D/I_G) reflects the graphitization degree of carbon materials, and the corresponding values are shown in Table 1. It appears that the I_D/I_G value of CSC was 0.91, which is lower than all the KOH activated samples. The lower I_D/I_G value of CSC is attributed to its underdeveloped porous structure. As we know, the lower the I_D/I_G value, the higher the graphitization degree, and the less disordered carbon [49, 50]. With the increase of KOH/C ratio, the I_D/I_G value of CSCK-800-*x* samples increased, demonstrating the more disordered carbon. Among CSCK-T-2, the CSCK-800-2 possessed the highest I_D/I_G value of 1.07,indicating that CSCK-800-2 would possess highest defect degree and more active sites which contributes to high energy storage [46].

3.1.4 BET analysis

Figure 4 shows the N2 adsorption − desorption isotherms and pore size distributions of all samples. The samples after KOH activation are shown as type I and IV with the H_4 hoop, which demonstrates the presence of hierarchical micro- and mesopore architecture (Fig. 4(a) and 4(c)) [51, 52]. Such hierarchical pore structure provides large surface area of the electrode/electrolyte interface for ions adsorption and

transport [53, 54]. However, CSC only shows a type-III adsorption isotherm with rapid adsorption under high relative pressure ($P/P_0 > 0.8$), indicating that CSC mainly has macroporous structure and a limited number of mesopores [55].

The pore size distribution curves of carbon samples shown in Fig. 4(b) and 4(d) are consistent with the N_2 adsorption/desorption analysis. It can be seen that in all CSCK-T-*x* samples, micropores are still the major part coexisting with a few of small mesopores (4 nm). However, with increasing the KOH/C ratio to > 2 large mesopores with size of 14 nm are gradually created. Importantly, the small mesopores ensure a high surface area and enough active sites to establish countless double electric layers, thus improving the charge storage capacity of supercapacitors [20].The mesopores with diameters between 10 and 50 nm provide shorter ion-transport channels with a minimized inner-pore resistance [18]. The presence of double mesopores could result in high retention capability, since they could serve as both electrolyte reservoirs and highways for efficient electrolyte transport, which contributes to improved rate performance.

Based on the above analysis, the process of the porous carbon formation was proposed as follows. The carbon was activated with KOH at high temperature, and a series of redox reactions take place to etch the carbon frame and generate H_2, CO_2 and CO which were occupied by the resultant potassium compounds and then washed with distilled water and diluted HCl and boost number of micropores and small mesopores effectively. The activation mechanism was based on the following equations [21].

$$6KOH + 2C \rightarrow 2K + 3H_2 + 2K_2CO_3$$

1

$$K_2CO_3 \rightarrow K_2O + CO_2$$

2

$$CO_2 + C \rightarrow 2CO$$

3

$$K_2CO_3 + 2C \rightarrow 2K + 3CO$$

4

$$K_2O + C \rightarrow 2K + CO$$

5

The specific surface area (S_{BET}) and total pore volume (V_{total}) parameters of all samples were summarized in Table 1. The CSC exhibits a low surface area (S_{BET}=340.4$m^2 \cdot g^{-1}$), whereas the CSCK-T-*x* samples exhibit much higher surface areas (865.3~2143.6 $m^2 \cdot g^{-1}$), which confirms that KOH makes a

vital contribution to the formation of the pore structure. As the KOH/C ratio and activation temperature increases, the S_{BET} and V_{total} rapidly increases and then decreases, reaches a maximum (2143.6 $m^2 \cdot g^{-1}$ and 1.34 $cm^3 \cdot g^{-1}$) at 800 °C with a KOH/C ratio of 2. In addition, the change of micropores area (S_{micro}) of CSCK-T-*x* showed peaklike shape, increasing rapidly from 669.1 $m^2 \cdot g^{-1}$ at 700 °C to 1299.2 $m^2 \cdot g^{-1}$ at 800 °C, and then decreased to 1067.4 $m^2 \cdot g^{-1}$ at 900 °C. As we know, micropores play a key role in the formation of a double layer of activated carbon. The decrease in micropores area at 900 °C indicated that some of micropores were transformed into mesopores and macropores at higher activation temperature [56].

Table 1 Summary of the structure parameters for all samples

Samples	S_{BET} ($m^2 \cdot g^{-1}$)	S_{mic} ($m^2 \cdot g^{-1}$)	V_{total} ($cm^3 \cdot g^{-1}$)	I_D/I_G	R_s (Ω)	R_{ct} (Ω)
CSC	340.4	56.7	1.22	0.91	1.20	0.38
CSCK-700-2	865.3	669.1	0.53	0.94	0.92	0.18
CSCK-800-0.5	1324.5	787.6	0.88	1.04	1.12	0.19
CSCK-800-1	1794.2	1171.9	1.07	1.05	1.05	0.12
CSCK-800-2	2143.6	1299.2	1.34	1.07	0.81	0.11
CSCK-800-3	1928.8	1244.4	1.44	1.11	1.10	0.18
CSCK-900-2	1634.7	1067.4	0.97	0.97	1.07	0.17

3.1.5 XPS analysis

The surface elements of CSCK-800-2 are measured by XPS, corresponding test results as shown in Fig. 5. As can be seen from the XPS full scan spectrum (Fig. 5(a)) there are two peaks at around 284 and 532 eV that correspond to the C 1s peak of sp^2 carbon and the O 1s spectrum. As shown in Fig. 5(b) detailed bonding configurations of carbon atoms can be obtained from the high resolution C 1s spectra. The C 1s shows three peaks of C–C (285 eV), C–O (285.9 eV), O = C–O (288.4 eV) [57], which indicates the presence of functional carbon in the sample [58]. While, the O1s (Fig. 5(c)) consists of two peaks, which can be attributed to C = O (531.2eV) and C–O (532.7eV) [57]. These chemical bonds can improve the wettability of electrode materials surface, reduce the charge transfer resistance and may afford stable pseudo-capacitance via faradic reactions [57, 59].

3.2 Electrochemical performance in a three-electrode test

The electrochemical performances of CSC and CSCK-T-*x* samples were characterized by CV, GCD, and EIS in 6M KOH aqueous electrolyte using a three-electrode system. Figure 6(a) and 6(b) exhibits the CV curves of all samples at the scan rate of 50 $mV \cdot s^{-1}$. All of CV curves reveals the typical rectangular

shape, which can be attributed to the EDLC behavior [60]. The area enclosed by the CV curves represents capacitance [61]. The area of CSCK-800-2 is the largest, indicating the best specific capacitance. Figure 6(e) shows the CV curves of CSCK-800-2 at various scan rates in detail, and the CV curves of other samples at different scan rates from 5 to 200 $mV{\cdot}s^{-1}$ were also presented in Fig. S1. It can be observed that the CV curves of CSCK-800-2 remained a rectangle-like shape within the scanning rate (5-200 $mV{\cdot}s^{-1}$) without distinct deformation even at 200 $mV{\cdot}s^{-1}$, suggesting the rapid transfer of charge with good rate capability [62].

Figure 6(c) and 6(d) illustrates the GCD curves of all samples at the current density of 0.5 $A{\cdot}g^{-1}$. The curves show a triangular shape, which reflect the excellent electrochemical reversibility of the electrode. CSCK-800-2 shows the longest discharge time among all samples, demonstrating that CSCK-800-2 can adsorb/desorb more electrolyte ions in the charging and discharging process with outstanding capacitance performance [63]. This is due to the etching of KOH, many micropores and mesopores are increased on the surface of the pristine CSC, which can not only improve the specific surface area of the material, but also conducive to the diffusion and penetration of electrolyte ions and charge transmission, which plays a positive role in improving the electrochemical performance of SCs. It can be seen from Fig. 6(c) that the specific capacitance increases with the increase of KOH/C ratio. When the ratio of KOH/C is 2:1, the capacitance reaches the maximum value. Further increasing the amount of KOH will not increase the capacitance. The trend of specific capacitance is consistent with that of specific surface area. It is noteworthy that of all the CSCK-T-2 samples, CSCK-700-2 shows the lowest specific surface area, but its specific capacitance was higher than CSCK-900-2, which can be interpreted that the capacitance performance depends not only on the specific surface area but also on the reasonable pore size distribution. The capacitance performance of the CSCK-800-2 at the different current density was further evaluated by GCD test, and the corresponding curves were shown in Fig. 6(f) and the GCD curves for other samples are shown in Fig. S2. In particular, all GCD curves exhibit symmetrical triangles even at 20 $A{\cdot}g^{-1}$, demonstrating the excellent electrochemical performance [64]. Figure 6(g) shows the effect of the current density on gravimetric specific capacitance of the CSC and CSCK-800-2 samples calculated from the GCD curves. In detail, the specific capacitance of CSC maintains 150.3 and 75.6 F g^{-1} at 0.5 $A{\cdot}g^{-1}$ and 20 $A{\cdot}g^{-1}$ with capacitance retention of 50.3%. In contrast, good rate capability is observed in CSCK-800-2. It displays gravimetric specific capacitance of 317.0 and 216.0 $F{\cdot}g^{-1}$ at 0.5 and 20 $A{\cdot}g^{-1}$ with capacitance retention of 68.1%, respectively. The specific capacitance is 2.1 times higher than that of pristine coconut shell based commercial activated carbon at $0.5A{\cdot}g^{-1}$, which attributed to the presence of double mesopores(4 and 14 nm), as they could serve both as electrolyte reservoirs and as highways for efficient electrolyte transport, contributing to improved rate performance. The supercapacitor performance of CSCK-800-2 is superior to that of biomass-derived materials reported in literature (Table 2). Therefore, coconut shell-derived hierarchical porous carbon is an ideal electrode material with potential application prospect in SCs.

Figure 6(h) exhibits the Nyquist plots of all samples. In the low frequency region, all the samples showed nearly vertical lines, demonstrating ideal capacitive behavior. The equivalent series resistance (Rs) is

influenced by the contact resistance between the active material and current collector and the overall electrolyte resistance in solution [65]. It can be seen that the Rs of the CSC was about 1.2 Ω, which is 1.5 times that of CSCK-800-2 (0.8Ω). The localized graphitized structure of CSCK-800-2 contributes to the lower Rs. The charge-transfer resistance (R_{ct}) mainly comes from the faradaic reaction between the interfaces of electrode and electrolyte [30, 66]. As can be observed from Table 1, all the CSCK-T-*x* samples show low R_{ct} value (0.11∼0.19 Ω) than that of CSC (0.38 Ω), demonstrating small internal resistance, low ions transfer resistance, and excellent electrical conductivity [67, 68]. High specific surface area can intensify the charge transfer within the microporous of CSCK-T-*x* electrodes and lead to low Rct values.

Table 2 Comparision of elctrochemical performance of biomass-derived carbon materials.

Sample	C($F \cdot g^{-1}$)/Current density($A \cdot g^{-1}$)	Electrolye ($mol \cdot L^{-1}$)	Cyclability /Cycle	Rate capability (from a A/gto b A/g)	Ref
Shiitake mushrooms	306/1	6M KOH	95.7%/15000	77%(1–30)	[69]
Glucose	289/1	6MKOH	119.5%/5000	> 51.9(1 to 10)	[70]
Pomelo mesocarps	245/0.5	2M KOH	96.5%/10000	72%(0.5–20)	[71]
Borassus flabellier	238/1	1M KOH	90.2%/1000	98.4(1 to 5)	[72]
Lignin	268/0.5	6M KOH	93%/10000		[73]
Eggshell membranes	247.1/0.2	6M KOH	100%/10000	75.2%(0.2–10)	[74]
Cotton derived-carbon	180/0.5	6M KOH	95%/5000	92%(0.5–10)	[75]
Willow catkin	298/0.5	6M KOH	98%10000	78.2%(0.5–50)	[76]
Glucose with waste water	275/0.5	6M KOH		65.4%(0.5–20)	[77]
Coconut shell carbon	317/0.5	6M KOH	99.7%/10000	68%(0.5 to 20)	This work

3.3 Electrochemical performance in a two-electrode test

A symmetrical two-electrodes SC was assembled by CSCK-800-2 and the capacitive performance was measured in 6 M KOH (Fig. 7). As can be seen from Fig. 7(a), the nearly ideal rectangular shape of CV

curves demonstrates a typical EDLCs behavior. The CV curves retain quasi-rectangular shape without distinct deformation even at a high scan rate of 200 $mV \cdot s^{-1}$, suggesting its high reversibility and fast transportation of charge [78]. As shown in Fig. 7(b), all GCD curves exhibit similar equilateral triangle shape and the deformation can be ignored even at 20 $A \cdot g^{-1}$, also indicating its good electrochemical performance. The specific capacitance was calculated to be 97.8 $F \cdot g^{-1}$ at 0.5 $A \cdot g^{-1}$. It is observed from Fig. 7(c), the energy density was 13.6 $Wh \cdot kg^{-1}$ at a high power density of 250 $W \cdot kg^{-1}$. When the power density was increased to 10 $kW \cdot kg^{-1}$, the energy density decreased to 8.6 $Wh \cdot kg^{-1}$. This performance is significantly better than those reported carbon materials (Fig. 7(c)) [35, 55, 79–82]. Moreover, 99.7% of the initial capacitance can still be maintained at 5 $A \cdot g^{-1}$ after 10000 cycles of the CSCK-800-2-based symmetrical SC demonstrates that it has the potential of practical application with outstanding cycling stability (Fig. 7(d)). All in all, the coconut shell-derived porous carbon is an excellent and potential alternative electrode material with desirable electrochemical performance for SCs.

Conclution

In summary, a simple one-step KOH activation approach to prepare a cost-effective coconut shell-derived hierarchical porous carbon for high-performance supercapacitor was described. The effects of carbonization temperature and KOH/C ratio on the structure and electrochemical properties were studied systematically, with the aim to design a low-cost biomass carbon material for efficient supercapacitor. It is proved that the KOH activation can generate mesopores mainly at 4 nm and a small amount near 14 nm. The synthesized CSCK-800-2, which possessed unique hierarchical porous with an ultra-high surface of 2143.6 $m^2 \cdot g^{-1}$, exhibited the best supercapacitor performance because of the four characteristics (micipores could increase surface area to ensure high energy storage capacity, small mesopores for fast ion transfer, large mesopores shorten ion-transport channels with a minimized inner-pore resistance, and localized graphitic structure can enhance conductivity). It delivers high specific capacitances up to 317 $F \cdot g^{-1}$ at a current density of 0.5 $A \cdot g^{-1}$, and maintains high capacitance retention of 68.1% at 20 $A \cdot g^{-1}$. The energy density of 13.5 $Wh \cdot kg^{-1}$ at a power density of 250 $W \cdot kg^{-1}$ can be achieved. Moreover, the capacitance loss is kept below 0.3% after 10000 charge – discharge cycles at 5 A g^{-1}. The coconut shell-derived porous carbon is proved to be a promising, low cost and attractive electrochemical material.

Declarations

Author contributions

Yutong Zhao: Conceptualization, Methodology, Writing – original draft, Formal analysis, Validation, Project administration. Yuanyuan Wang: Validation, Investigation. Yanxiu Liu: Formal analysis. Huan Wang: Funding acquisition. Hua Song: Writing review & editing, Supervision, Project administration, Funding acquisition.

Competing Interests

The authors have no relevant financial or non-financial interests to disclose.

Funding

The authors did not receive support from any organization for the submitted work.

Data Availability Statement

All data generated or analysed during this study are included in this published article [and its supplementary information files].

Acknowledgements

We are grateful for financial support from National Natural Science Foundation of China (22008134).

References

1. J. Deng, M.M. Li, Y. Wang, Green Chem. 18, 18 (2016). http://dx.doi.org/10.1039/c6gc01172a
2. L. Wei, G. Yushin, Nano Energy 1, 4 (2012). http://dx.doi.org/10.1016/j.nanoen.2012.05.002
3. L. Zhou, H. Cao, S.Q. Zhu, L.R. Hou, C.Z. Yuan, Green Chem. 17, 4 (2015). http://dx.doi.org/10.1039/c4gc02032d
4. S.H. Yue, H. Tong, L. Lu, W.W. Tang, W.L. Bai, F.Q. Jin, Q.W. Han, J.P. He, J. Liu, X.G. Zhang, J. Mater. Chem. A 5, 2 (2017). http://dx.doi.org/10.1039/c6ta09128h
5. J. Yan, W. Sun, T. Wei, Q. Zhang, Z.J. Fan, F. Wei, J. Mater. Chem. 22, 23 (2012). http://dx.doi.org/10.1039/c2jm30221g
6. L.M. Santino, Y. Lu, S. Acharya, L. Bloom, D. Cotton, A. Wayne, J.M. D'Arcy, ACS Appl. Mater. Interfaces 8, 43 (2016). http://dx.doi.org/10.1021/acsami.6b09779
7. X. Tian, H.R. Ma, Z. Li, S.C. Yan, L. Ma, F. Yu, G. Wang, X.H. Guo, Y.Q. Ma, C.P. Wong, J. Power Sources 359, (2017). http://dx.doi.org/10.1016/j.jpowsour.2017.05.054
8. J. Du, L. Liu, Z.P. Hu, Y.F. Yu, Y. Zhang, S.L. Hou, A.B. Chen, ACS Sustainable Chem. Eng. 6, 3 (2018). http://dx.doi.org/10.1021/acssuschemeng.7b04396
9. L. Zhang, Q.Q. Xu, X. Wang, Q. Sun, F. He, W.D. Pan, H.B. Xie, RSC Adv 10, 68 (2020). http://dx.doi.org/10.1039/d0ra06780f
10. T.N.J.I. Edison, R. Atchudan, N. Karthik, P. Chandrasekaran, S. Perumal, P. Arunachalam, P.B. Raja, M.G. Sethuraman, Y.R. Lee , Surf. Coat. Technol. 416, 25 (2021). http://dx.doi.org/10.1016/j.surfcoat.2021.127150
11. Z.Q. Tong, Y.N. Yang, J.Y. Wang, J.P. Zhao, B.L. Su, Y. Li, J. Mater. Chem. A 2, 13 (2014). http://dx.doi.org/10.1039/c3ta14671e

12. J. Ryu, C.B. Park, Angew. Chem., Int. Ed. Engl. 48, 26 (2009). http://dx.doi.org/10.1002/anie.200900668
13. G.X. Huang, W.W. Kang, B.L. Xing, L.J. Chen, C.X Zhang, Fuel Process. Technol. 142, (2016). http://dx.doi.org/10.1016/j.fuproc.2015.09.025
14. J. Li, W.L. Liu, D. Xiao, X.H. Wang, Appl. Surf. Sci. 416, 15 (2017). http://dx.doi.org/10.1016/j.apsusc.2017.04.162
15. C. Liang, J.P. Bao, C.G. Li, H. Huang, C.L. Chen, Y. Lou, H.Y. Lu, H.B. Lin, Z. Shi, S.H. Feng, Microporous Mesoporous Mater. 251, (2017). http://dx.doi.org/10.1016/j.micromeso.2017.05.044
16. Q. Zhang, K.H. Han, S.J. Li, M. Li, J.X. Li, K. Ren, Nanoscale 10, 5 (2018). http://dx.doi.org/10.1039/c7nr07158b
17. H.L. Jin, X. Feng, J. Li, M. Li, Y.Z. Xia, Y.F. Yuan, C. Yang, B. Dai, Z.Q. Lin, J.C. Wang, J. Lu, S. Wang, Angew. Chem., Int. Ed. Engl. 58, 8 (2019). http://dx.doi.org/10.1002/anie.201813686
18. D.W. Wang, F. Li, M. Liu, G.Q. Lu, H.M. Cheng, Angew. Chem., Int. Ed. Engl. 47, 2 (2008). http://dx.doi.org/10.1002/anie.200702721
19. H.J. Liu, J. Wang, C.X. Wang, Y.Y. Xia, Adv. Energy Mater. 1, 6 (2011). http://dx.doi.org/10.1002/aenm.201100255
20. G.L. Zhang, T.T. Guan, N. Wang, J.C. Wu, J.L. Wang, J.L. Qiao, K.X. Li, Chem. Eng. J. 399, 1 (2020). http://dx.doi.org/10.1016/j.cej.2020.125818
21. J.C. Wang, S. Kaskel, J. Mater. Chem. 22, 45 (2012). http://dx.doi.org/10.1039/c2jm34066f
22. H. Zhang, G.P. Cao, Y.S. Yang, Z.N. Gu, Carbon 46, 1 (2008). http://dx.doi.org/10.1016/j.carbon.2007.10.023
23. Y. Huang, J.J. Liang, Y.S. Chen, Small 8, 12 (2012). http://dx.doi.org/10.1002/smll.201102635
24. J. Wei, D.D. Zhou, Z.K. Sun, Y.H. Deng, Y.Y. Xia, D.Y. Zhao, Adv. Funct. Mater. 23, 18 (2013). http://dx.doi.org/10.1002/adfm.201202764
25. O. Ioannidou, A. Zabaniotou, Renewable Sustainable Energy Rev. 11, 9 (2007). http://dx.doi.org/10.1016/j.rser.2006.03.013
26. Z.Q. Hao, J.P. Cao, Y. Wu, X.Y. Zhao, Q.Q. Zhuang, X.Y. Wang, X.Y. Wei, J. Power Sources 361, 1 (2017). http://dx.doi.org/10.1016/j.jpowsour.2017.06.086
27. H.B. Li, S. Liang, J. Li, L.J. He, J. Mater. Chem. A 1, 21 (2013). http://dx.doi.org/10.1039/c3ta10681k
28. L.H. Yin, Y. Chen, D. Li, X.Q. Zhao, B. Hou, B.K. Cao, Mater. Des. 111, 5 (2016). http://dx.doi.org/10.1016/j.matdes.2016.08.070
29. C.D. Ma, J. Gong, S. Zhao, X.G. Liu, X.Y. Mu, Y.H. Wang, X.C. Chen, T. Tang, Green Energy Environ. 7, 4 (2022). http://dx.doi.org/10.1016/j.gee.2020.12.004
30. K.L. Wang, Y.H. Cao, X.M. Wang, M.A. Castro, B. Luo, Z.R. Gu, J. Liu, J.D. Hoefelmeyer, Q.H. Fan, J. Power Sources 307, 1 (2016). http://dx.doi.org/10.1016/j.jpowsour.2016.01.008
31. V. Dhyani, T. Bhaskar, Renewable Energy 129, (2018). http://dx.doi.org/10.1016/j.renene.2017.04.035

32. C.W. Song, S.H. Wu, M.R. Cheng, P. Tao, M.H. Shao, G.R. Gao, Sustainability 6, 1 (2013). http://dx.doi.org/10.3390/su6010086
33. L. Li, S.Q. Liu, J.X. Liu, J. Hazard. Mater. 192, 2 (2011). http://dx.doi.org/10.1016/j.jhazmat.2011.05.069
34. K.W. Mas'udah, I.M.A. Nugraha, S. Abidin, A. Mufid, F. Astuti, Darminto, Am. Inst. Phys. 1725,1 (2016). http://dx.doi.org/10.1063/1.4945499
35. A. Jain, S.K. Tripathi, J. Renewable Sustainable Energy 6, 1 (2014). http://dx.doi.org/10.1063/1.4861889
36. K. Mensah-Darkwa, C. Zequine, P. Kahol, R. Gupta, Sustainability 11, 2 (2019). http://dx.doi.org/10.3390/su11020414
37. Q.T. Jiang, D.D. Liu, B. Liu, T. Zhou, J. Zhou, Molecules 24, 24 (2019). http://dx.doi.org/10.3390/molecules24244625
38. W. Xiong, M.X. Liu, L.H. Gan, Y.K. Lv, Y. Li, L. Yang, Z.J. Xu, Z.X. Hao, H.L. Liu, L.W. Chen, J. Power Sources 196, 23 (2011). http://dx.doi.org/10.1016/j.jpowsour.2011.07.083
39. K. Kuratani, K. Okuno, T. Iwaki, M. Kato, N. Takeichi, T. Miyuki, T. Awazu, M. Majima, T. Sakai, J. of Power Sources 196, 24 (2011). http://dx.doi.org/10.1016/j.jpowsour.2011.09.001
40. X.C. Jiang, F.Q. Guo, X.P. Jia, Y.B. Zhan, H.M. Zhou, L. Qian, J. Energy Storage 30, (2020). http://dx.doi.org/10.1016/j.est.2020.101451
41. S.W. Woo, K. Dokko, H. Nakano, K. Kanamura, J. Mater. Chem. 18, 14 (2008). http://dx.doi.org/10.1039/b717996k
42. W.J. Qian, F.X. Sun, Y.H. Xu, L.H. Qiu, C.H. Liu, S.D. Wang, F. Yan, Energy Environ. Sci. 7, 1 (2014). http://dx.doi.org/10.1039/c3ee43111h
43. T.Y. Wei, X.L. Wei, L.W. Yang, H.P. Xiao, Y. Gao, H.M. Li, J. Power Sources 331, 1 (2016). http://dx.doi.org/10.1016/j.jpowsour.2016.09.053
44. Y.W. Zhu, S. Murali, M.D. Stoller, K.J. Ganesh, W.W. Cai, P.J. Ferreira, A. Pirkle, R.M. Wallace, K.A. Cychosz, M. Thommes, D. Su, E.A. Stach, R.S. Ruoff, Science 332, 6037 (2011). http://dx.doi.org/10.1126/science.1200770
45. V. Sahu, S. Grover, B. Tulachan, M. Sharma, G. Srivastava, M. Roy, M. Saxena, N. Sethy, K. Bhargava, D. Philip, H. Kim, G. Singh, S.K. Singh, M. Das, R.K. Sharma, Electrochim. Acta 160, 1 (2015). http://dx.doi.org/10.1016/j.electacta.2015.02.019
46. X.J. Wei, J.S. Wei, Y.B. Li, H.L. Zou, J. Power Sources 414, 28 (2019). http://dx.doi.org/10.1016/j.jpowsour.2018.12.064
47. A. Bello, F. Barzegar, D. Momodu, J. Dangbegnon, F. Taghizadeh, N. Manyala, Electrochim. Acta 151, 1 (2015). http://dx.doi.org/10.1016/j.electacta.2014.11.051
48. J.S. Zhou, J. Lian, L. Hou, J.C. Zhang, H.Y. Gou, M.R. Xia, Y.F. Zhao, T.A.Strobel, L. Tao, F.M. Gao, Nat. Commun. 6, 8503 (2015). http://dx.doi.org/10.1038/ncomms9503

49. L.F. Chen, Z.H. Huang, H.W. Liang, W.T. Yao, Z.Y. Yu, S.H. Yu, Energy Environ. Sci. 6, 11 (2013). http://dx.doi.org/10.1039/c3ee42366b
50. S. Shanmugam, T. Osaka, Chem. Commun. 47, 15 (2011). http://dx.doi.org/10.1039/c1cc10361j
51. Y. Chen, M. Wang, M. Tian, Y.Z. Zhu, X.J. Wei, T. Jiang, S.Y. Gao, Nano Energy 42, (2017). http://dx.doi.org/10.1016/j.nanoen.2017.10.060
52. M. Tian, Y.Z. Zhu, D.L. Zhang, M. Wang, Y. Chen, Y.J. Yang, S.Y. Gao, Nano Energy 64, (2019). http://dx.doi.org/10.1016/j.nanoen.2019.103940
53. M. Sevilla, R. Mokaya, Energy Environ. Sci. 7, 4 (2014). http://dx.doi.org/10.1039/c3ee43525c
54. Y. Zhai, Y. Dou, D. Zhao, P. F. Fulvio, R. T. Mayes, S. Dai, Adv. Mater. 23, 42 (2011). http://dx.doi.org/10.1002/adma.201100984
55. W.X. Wang, H.Y. Quan, W.M. Gao, R. Zou, D.Z. Chen, Y.H. Dong, L. Guo, RSC Adv. 7, 27 (2017). http://dx.doi.org/10.1039/c7ra01043e
56. W.L. Zhang, M.Z. Zhao, R.Y. Liu, X.F. Wang, H.B. Lin, Colloids Surf., A 484, 5 (2015). http://dx.doi.org/10.1016/j.colsurfa.2015.08.030
57. B.J. Yu, Z.Z. Chang , C.Y. Wang, Mater. Chem. Phys. 181, 15 (2016). http://dx.doi.org/10.1016/j.matchemphys.2016.06.048
58. L. Wei, K. Tian, Y.Y. Jin, X.Y. Zhang, X. Guo, Microporous Mesoporous Mater. 227, (2016). http://dx.doi.org/10.1016/j.micromeso.2016.03.015
59. B.L. Xing, G.X. Huang, L.J. Chen, H. Guo, C.X. Zhang, W. Xie, Z.F. Chen, J. Porous Mater. 23, 1 (2015). http://dx.doi.org/10.1007/s10934-015-0056-0
60. D. Hulicova-Jurcakova, M. Seredych, G.Q. Lu, T.J. Bandosz, Adv. Funct. Mater. 19, 3 (2009). http://dx.doi.org/10.1002/adfm.200801236
61. F. Xu, R.J. Cai, Q.C. Zeng, C. Zou, D.C. Wu, F. Li, X. Lu, Y.R. Liang, R.W. Fu, J. Mater. Chem. 21, 6 (2011). http://dx.doi.org/10.1039/c0jm02044c
62. J.T. Jin, X.C. Qiao, F. Zhou, Z.S. Wu, L.F. Cui, H.B. Fan, ACS Appl. Mater. Interfaces 9, 20 (2017). http://dx.doi.org/10.1021/acsami.7b00617
63. X.L. Gao, W. Xing, J. Zhou, G.Q. Wang, S.P. Zhuo, Z. Liu, Q.Z. Xue, Z.F. Yan, Electrochim. Acta 133, 1 (2014). http://dx.doi.org/10.1016/j.electacta.2014.04.101
64. Y. Liu, L.J. Cao, J. Luo, Y.Y. Peng, Q. Ji, J.Y. Dai, J. Zhu, X.Q. Liu, ACS Sustainable Chem. Eng. 7, 2 (2018). http://dx.doi.org/10.1021/acssuschemeng.8b05947
65. D. Puthusseri, V. Aravindan, S. Madhavi, S. Ogale, Energy Environ. Sci. 7, 2 (2014). http://dx.doi.org/10.1039/c3ee42551g
66. K.L. Sun, S.H. Yu, Z.L. Hu, Z.H. Li, G.T. Lei, Q.Z. Xiao, Y.H. Ding, Electrochim. Acta 231, 20 (2017). http://dx.doi.org/10.1016/j.electacta.2017.02.078
67. J.L. Chang, Z.Y. Gao, X.R. Wang, D.P. Wu, F. Xu, X. Wang, Y. Guo, K. Jiang, Electrochim. Acta 157, 1 (2015). http://dx.doi.org/10.1016/j.electacta.2014.12.169

68. B.Y. Guan, Y. Lu, Y. Wang, M.H. Wu, X.W. Lou, Adv. Funct. Mater. 28, 10 (2018). http://dx.doi.org/10.1002/adfm.201706738
69. P. Cheng, S.Y. Gao, P.Y. Zang, X.F. Yang, Y.L Bai, H. Xu, Z.H Liu, Z.B. Lei, Carbon 93, (2015). http://dx.doi.org/10.1016/j.carbon.2015.05.056
70. Z.J. Zhang, Q. Wang, Y.Q. Zhu, X.Y. Chen, Carbon 100, (2016). http://dx.doi.org/10.1016/j.carbon.2016.01.046
71. H. Peng, G.F. Ma, K.J. Sun, Z.G. Zhang, Q. Yang, Z.Q. Lei, Electrochim. Acta 190, 1 (2016). http://dx.doi.org/10.1016/j.electacta.2015.12.195
72. M. Sivachidambaram, J.J. Vijaya, L.J. Kennedy, R. Jothiramalingam, H. Al-Lohedan, M.A. Munusamy, E. Elanthamilan, J.P. Merlin, New J. Chem. 41, 10 (2017). http://dx.doi.org/10.1039/c6nj03867k
73. Z.Z. Chang, B.J. Yu, C.Y. Wang, J. Solid State Electrochem. 20, 5 (2016). http://dx.doi.org/10.1007/s10008-016-3146-2
74. M. Karuppannan, Y. Kim, Y.E. Sung, O.J. Kwon, J. Appl. Electrochem. 49, 1 (2018). http://dx.doi.org/10.1007/s10800-018-1276-1
75. L. Chen, T. Ji, L.W. Mu, J.H. Zhu, Carbon 111, (2017). http://dx.doi.org/10.1016/j.carbon.2016.10.054
76. Y.J. Li, G.L. Wang, T. Wei, Z.J. Fan, P. Yan, Nano Energy 19, (2016). http://dx.doi.org/10.1016/j.nanoen.2015.10.038
77. Y.N. Lin, H. Chen, Y.L. Shi, G. Wang, L. Chen, F. Wang, S.Q. Li, F. Yu, L.L. Zhang, Glob. Chall. 3, 11 (2019). http://dx.doi.org/10.1002/gch2.201900043
78. M. Chen, Z.F. Zhou, L. Zhao, M. Lin, Q.N. Guo, M.W. Li, Water 10, 6 (2018). http://dx.doi.org/10.3390/w10060779
79. S.Y. Bai, G.Q. Tan, X.Q. Li, Q. Zhao, Y. Meng, Y.J. Wang, Y.Z. Zhang, D. Xiao, Chem. - Asian J. 11, 12 (2016). http://dx.doi.org/10.1002/asia.201600303
80. J. Yang, Y.F. Liu, X.M. Chen, Z.H. Hu, G.H. Zhao, Acta Phys.-Chim. Sin. 24, 1 (2008). http://dx.doi.org/10.1016/s1872-1508(08)60002-9
81. Z. Ling, Z.Y. Wang, M.D. Zhang, C. Yu, G. Wang, Y.F. Dong, S.H. Liu, Y.W. Wang, J.S. Qiu, Adv. Funct. Mater. 26, 1 (2016). http://dx.doi.org/10.1002/adfm.201504004
82. M.h. Jiang, X.F. Yu, R.R. Gao, T. Yang, Z.X. Xu, L.H. Cao, Nano 15, 07 (2020). http://dx.doi.org/10.1142/s1793292020500964

Scheme

Scheme 1 is available in Supplementary Files section.

Figures

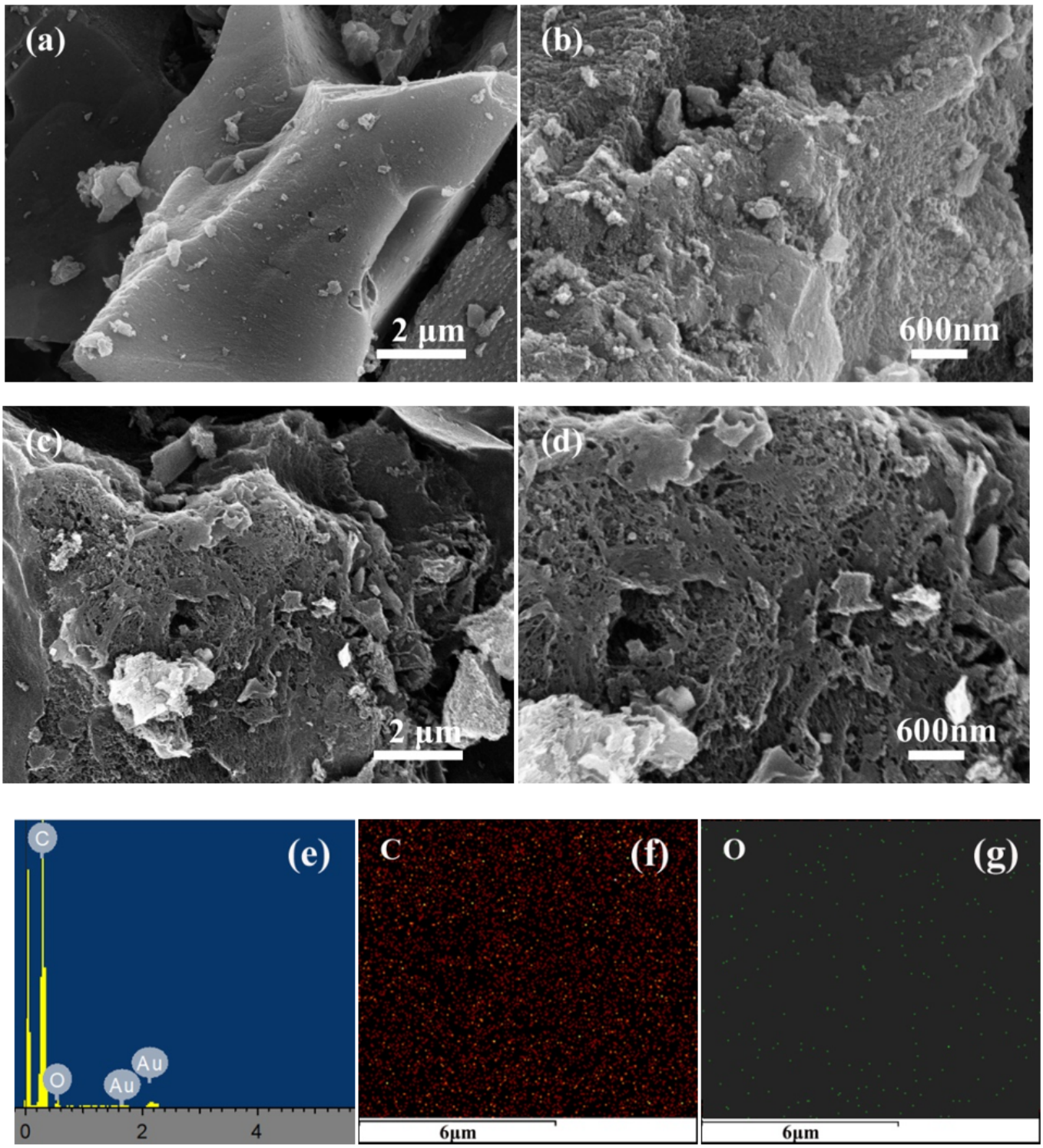

Figure 1

SEM images of **a-b** CSC, **c-d** CSCK-800-2, **e** EDX spectrum and **f-g** element mapping analyses of CSCK-800-2

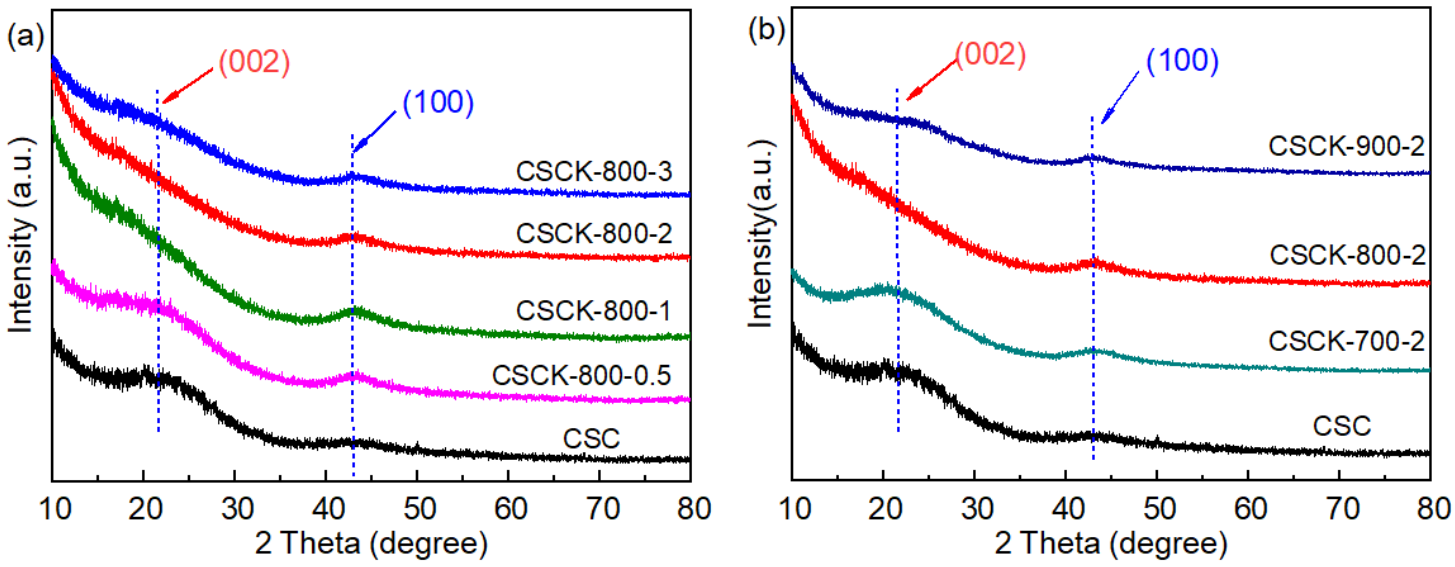

Figure 2

XRD curves of **a** pristine CSC and CSCK-800-*x*, **b** CSC and CSCK-T-2

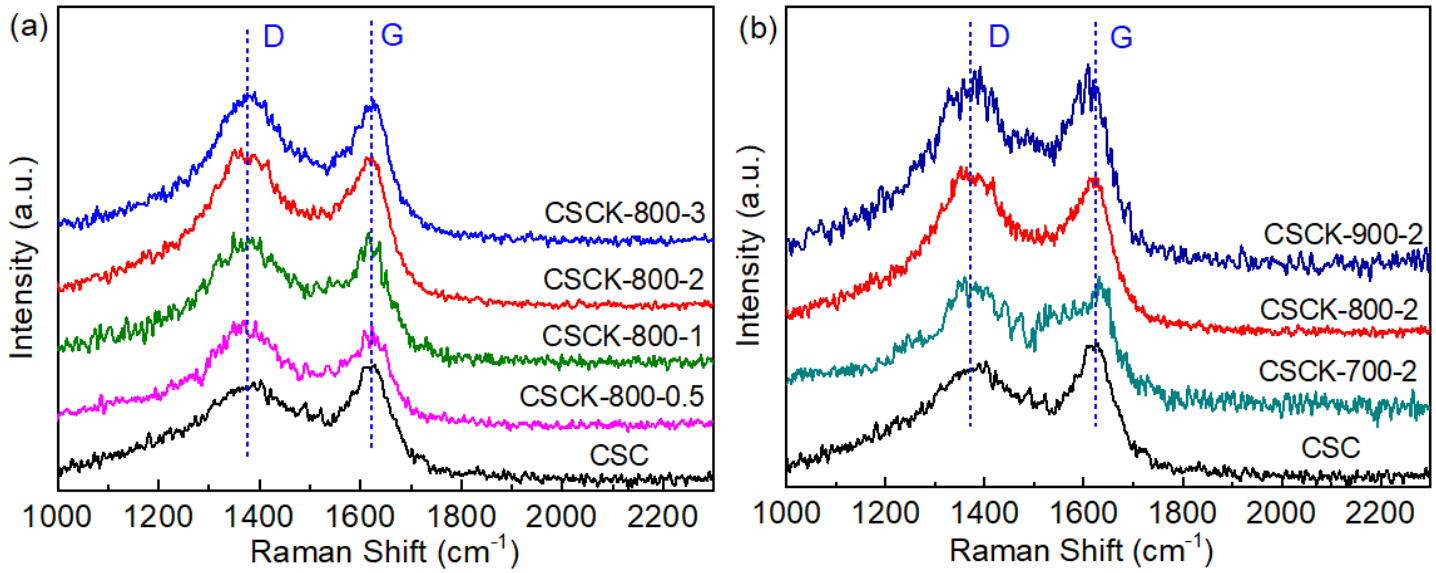

Figure 3

Raman curves of **a** pristine CSC and CSCK-800-*x*, **b** CSC and CSCK-T-2

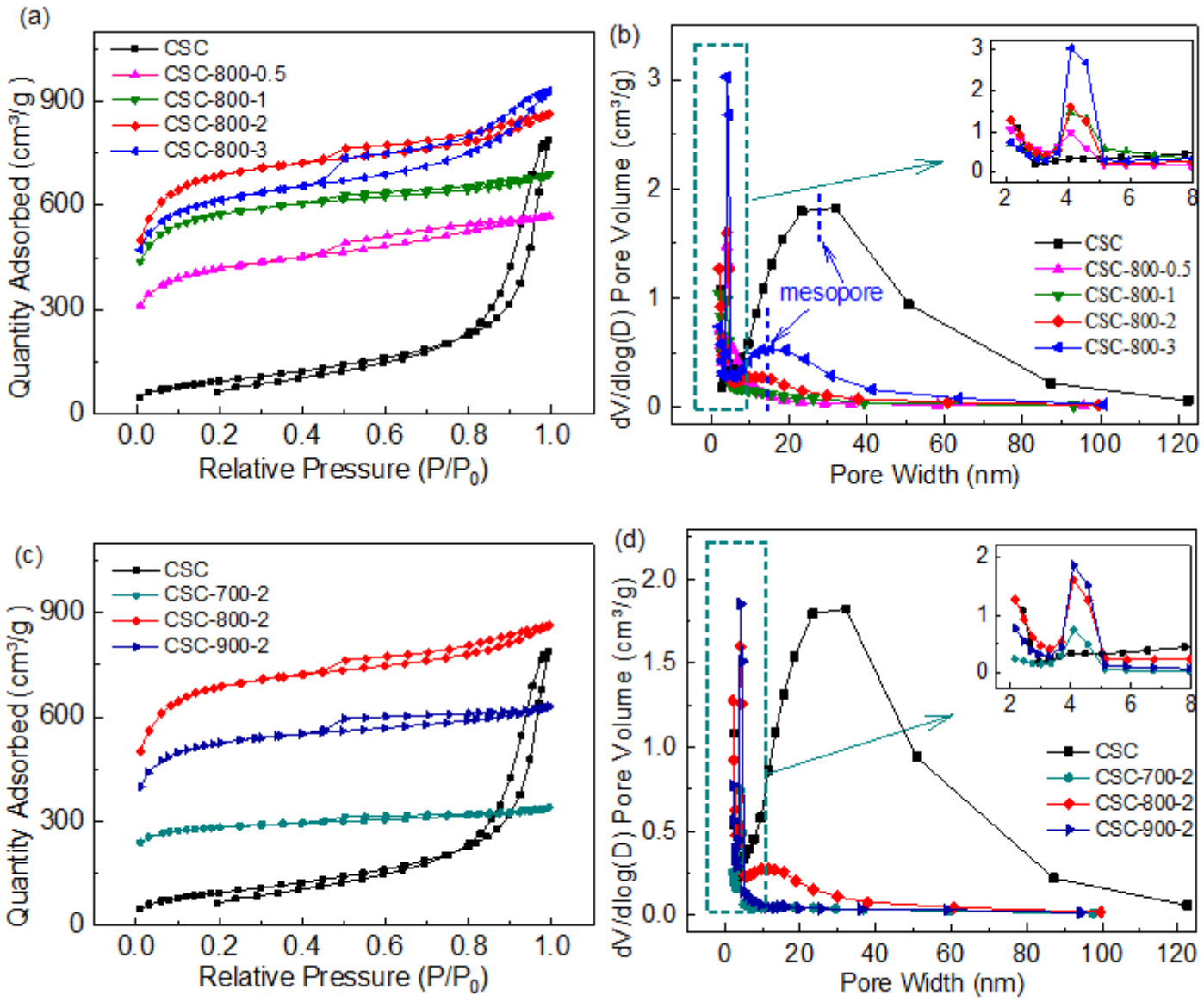

Figure 4

a and **c** Nitrogen adsorption/desorption isotherms, **b** and **d** pore size distributions of all samples

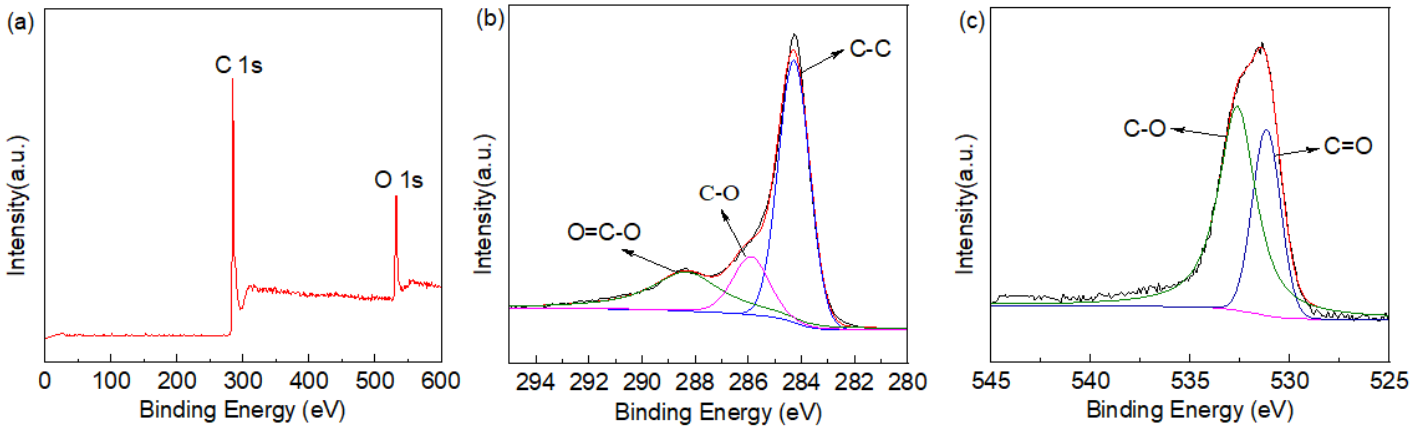

Figure 5

XPS survey spectra of **a** CSCK-800-2, **b** C 1s spectrum and **c** O 1s spectrum

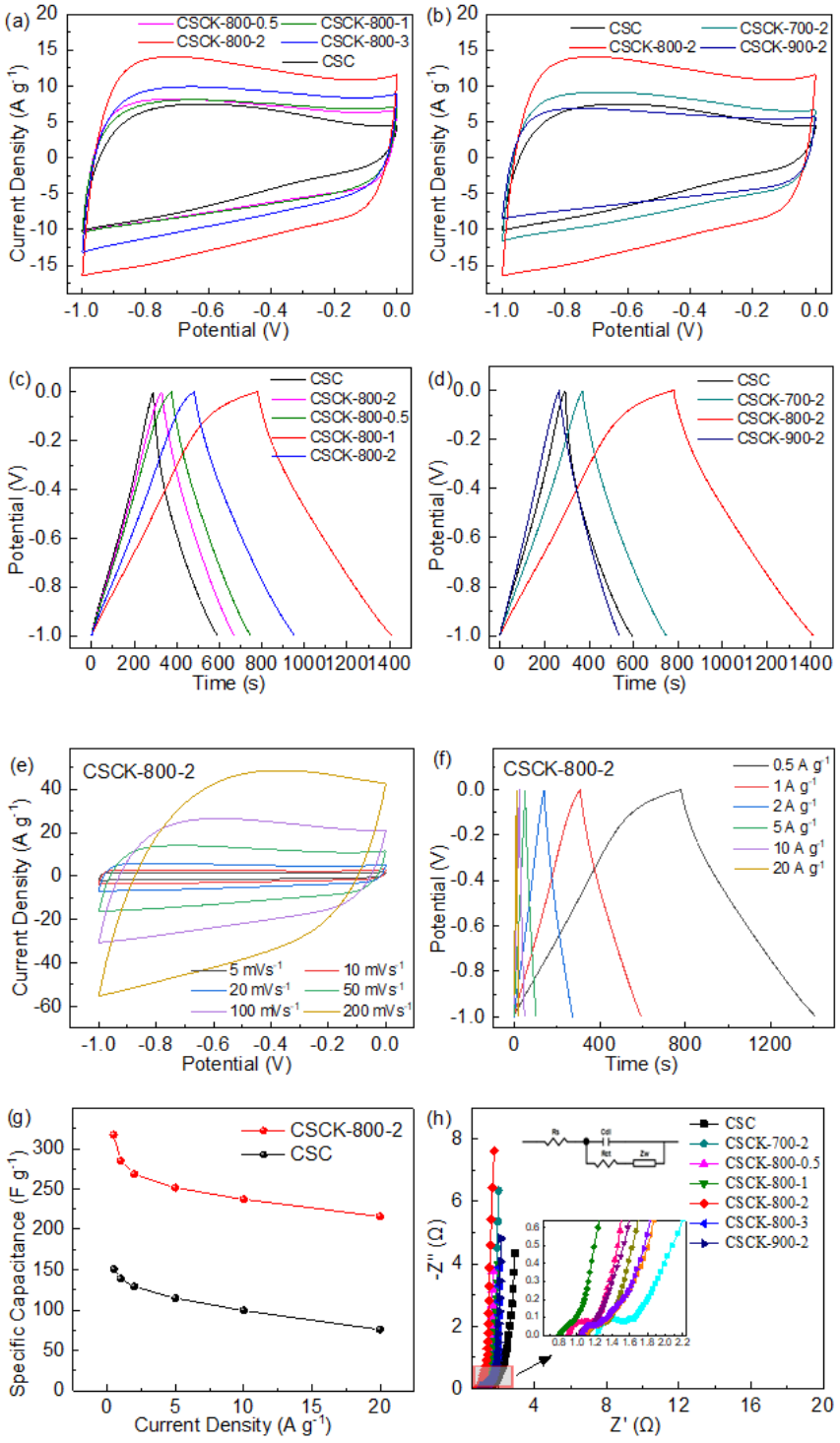

Figure 6

Electrochemical performance of all samples in a three-electrode system: **a-b** CV curves at 50 mV·s^{-1}, **c-d** GCD curves at a current density of 0.5 A·g^{-1}, **e** CV curves of CSCK-800-2 at different scan rates, **f** GCD curves of CSCK-800-2 at different current density, **g** variation of specific capacitance with current density of CSC and CSCK-800-2, **h** Nyquist plots

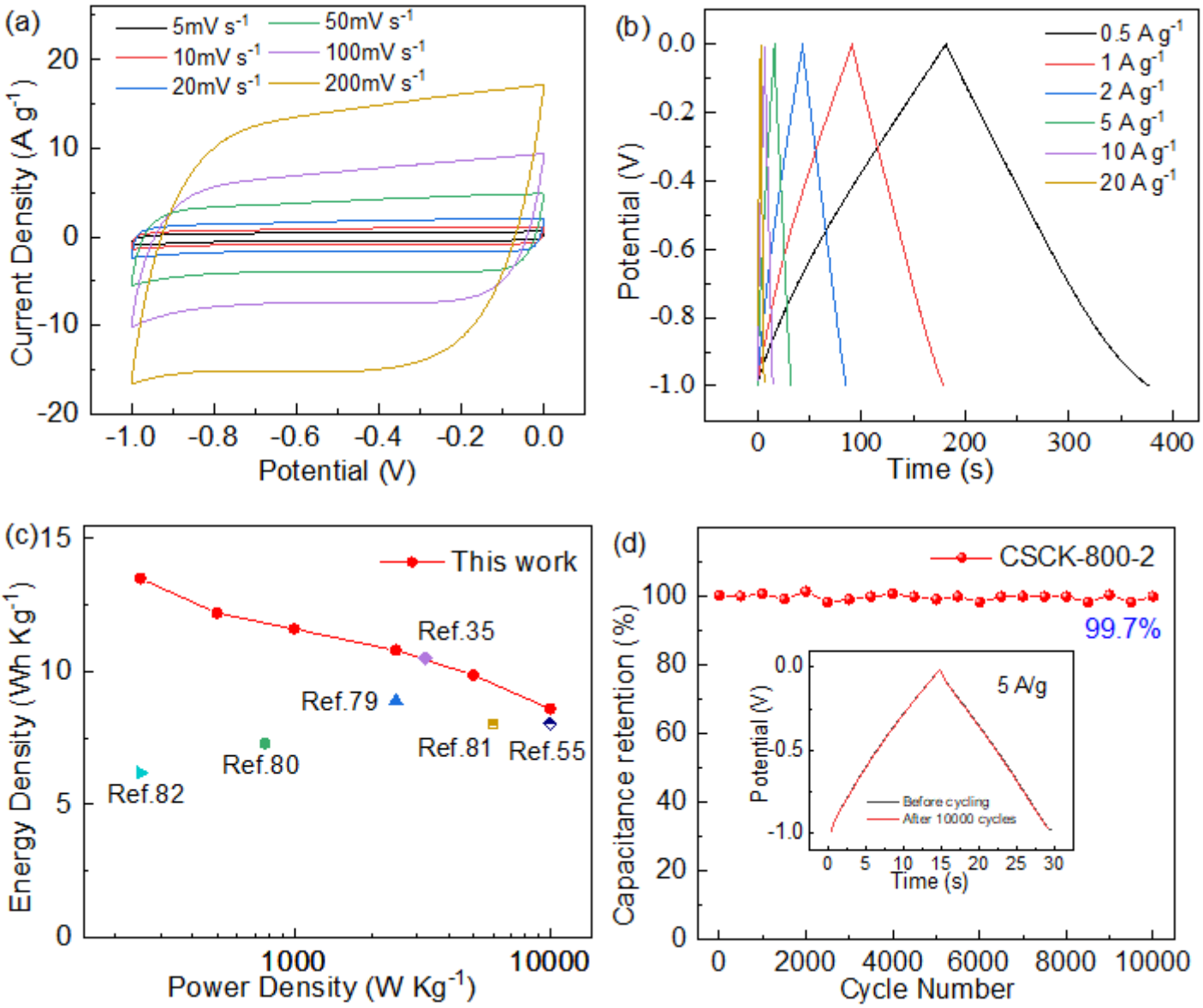

Figure 7

Electrochemical performances of a symmetric supercapacitor prepared by CSCK-800-2 in 6 M KOH electrolyte. **a** CV curves at 5~200 mV s^{-1} scan rates, **b** GCD curves at 5~20A·g^{-1}current densities, **c** Comparison of Ragone plots of the CSCK-800-2 with other work, **d** The capacitance retention ratio of CSCK-800-2-based SC after 10000 charge–discharge cycles at 5 A·g^{-1}

Supplementary Files

This is a list of supplementary files associated with this preprint. Click to download.

- SupplementaryInformation.docx
- Scheme1.png